

GaAs to Si Direct Wafer Bonding at $T \leq 220^\circ\text{C}$ in Ambient Air via Nano-BondingTM and Surface Energy Engineering (SEE)

Aashi R. Gurijala (✉ agurijal@asu.edu)

Arizona State University <https://orcid.org/0000-0002-4591-1081>

Amber A. Chow

Arizona State University

Shaurya Khanna

Arizona State University

Nikhil C. Suresh

Arizona State University

Pranav V. Penmatcha

Arizona State University

Siddarth V. Jandhyala

Arizona State University

Mohammed Sahal

Arizona State University

Wesley Peng

Arizona State University

Thilina N. Balasooriya

Arizona State University

Sukesh Ram

Yale University

Timoteo Diaz

Arizona State University

Michelle Bertram

Arizona State University

Christian E. Cornejo

Arizona State University

Karen L. Kavanagh

Simon Fraser University

Robert J. Culbertson

Arizona State University

Nicole Herbots

Research Article

Keywords: Direct Wafer Bonding, Nano-Bonding, Surface Energy Engineering, Native Oxides, Solar Cell

Posted Date: April 27th, 2021

DOI: <https://doi.org/10.21203/rs.3.rs-425834/v1>

License:  This work is licensed under a Creative Commons Attribution 4.0 International License.

[Read Full License](#)

Abstract

When different semiconductors are integrated into hetero-junctions, native oxides generate interfacial defects and cause electronic recombination. Two state-of-the-art integration methods, hetero-epitaxy and Direct Wafer Bonding (DWB), require temperatures $> 400^{\circ}\text{C}$ to reduce native oxides. However, $T > 400^{\circ}\text{C}$ leads to defects due to lattice and thermal expansion mismatches. In this work, DWB temperatures are lowered via Nano-Bonding™ (NB) at $T \leq 220^{\circ}\text{C}$ and $P \leq 60 \text{ kPa}$ (9 psi). NB uses Surface Energy Engineering (SEE) at 300K to modify surface energies (γ^{T}) to far-from-equilibrium states, so cross-bonding occurs with little thermal activation and compression. SEE modifies γ^{T} and hydro-affinity (HA) via chemical etching, planarization, and termination that are optimized to yield 2-D Precursor Phases (2D-PP) metastable in ambient air and highly planar at the nano- and micro- scales. Complementary 2D-PPs nano-contact via carrier exchange from donor 2D-PP surfaces to acceptor ones. Here, NB models and SEE are applied to the DWB of GaAs to Si for photo-voltaics. SEE modifies (1) the initial $\gamma^{\text{T}0}$ and HA^0 measured via Three Liquid Contact Angle Analysis, (2) the oxygen coverage measured via High Resolution Ion Beam Analysis, and (3) the oxidation states measured via X-Ray Photoelectron Spectroscopy. SEE etches hydrophobic GaAs oxides with $\gamma^{\text{T}} = 33.4 \pm 1 \text{ mJ/m}^2$, and terminates GaAs (100) with H^+ , rendering GaAs hydrophilic with $\gamma^{\text{T}} = 60 \pm 2 \text{ mJ/m}^2$. Similarly, hydrophilic Si native oxides are etched into hydrophobic SiO_4H_2 . H^+ - GaAs nano-bonds reproducibly to Si, as measured via Surface Acoustic Wave Microscopy, validating the NB model and SEE design.

1 Introduction

1.1 Photo-Voltaic Conversion Efficiency Limits in Single Crystal Solar Cells

Photo-Voltaic (PV) Conversion Efficiency (PV-CE) is the percentage of solar energy converted into usable electricity by a solar cell. Theoretically, the absolute thermodynamic maximum for solar PV-CE is 68.7% [1, 2]. As of 2021, 90% of the solar cell market is constituted of mono-crystalline Si solar cells. The maximum reported practical PV-CE is 26.7%- about a third of that limit. Moreover, it took 45 years to double the PV-CE of Si solar cells from 13–26.7% [1–4]. Worse, 26.7% is only a few % shy of the theoretical maximum of 30.1% for single crystal Si solar cells [1]. What can be done to improve PV-CE? The key limiting factor in the PV-CE of mono-crystalline cells is their narrow absorption range. The leading material for terrestrial photo-voltaics is Si and for space photo-voltaics is GaAs. Each absorbs a different portion of the solar spectrum. Si-only solar cells have a maximum theoretical PV-CE of 30.1% because they absorb the 0.4–1.1 μm portion of the solar spectrum, while GaAs-only solar cells are more efficient with a maximum theoretical PV-CE of 35% instead of 30.1%. This is because GaAs absorbs the solar spectrum in a range almost twice as large as that of Si, from 0.8 to 2 μm [1].

1.2 Multi-junction Solar Cells Overcome Mono-crystalline Solar Cell PV-CE Limitations

Forty-five years of photo-voltaics research has established the advantages of combining two materials into the so-called "tandem solar cell", or more than two semiconductor surfaces into multi-junction solar cells [1]. In the last two decades, multi-junction tandem solar cells such as GaInP/GaAs/Ge

(1.82/1.42/0.67 eV) and lattice-matched triple-junction cells have achieved efficiencies of over 30%. GaAs dominates space applications because of its higher PV-CE, despite higher costs [5–7].

Prohibitive costs and scarcity of rare earth and semimetals limit the availability of materials for solar cells in terrestrial applications. Hence, for the terrestrial solar market, including solar power plants, only GaAs/Si tandem solar cells can currently achieve the right combination of efficiency and costs.

A GaAs/Si tandem cell absorbs the solar spectrum from 0.4 to 2 μm , resulting in a higher PV-CE than Si or GaAs alone. Theoretically, a GaAs/Si tandem cell can achieve a PV-CE of up to 42.9% without solar concentration. This is a 50% improvement over single junction Si solar cells and a 14% improvement over single-junction GaAs solar cells [1]. Thus, even at about 2/3 of the theoretical maximum, GaAs/Si tandem solar cells are a very significant improvement over single-junction, Si solar cells.

1.3 Challenges to Overcome in GaAs/Si Tandem Solar Cell Technology

In 2019, the National Renewable Energy Laboratory certified experimentally that GaAs/Si tandem solar cells have reached a PV-CE of 32.9% [1]. Even after 20 years, there is still a very significant gap of 10% in theoretical versus experimental PV-CE results due to defects on the GaAs/Si interface. In other words, 30% of the possible increase of PV-CE is still unrealized.

Since 1989, the PV-CE of GaAs/Si solar cells has increased from 28% by only 5% [1]. The two leading technologies for integrating GaAs to Si are (1) hetero-epitaxy of GaAs on Si via various thin-film deposition techniques and (2) Direct Wafer Bonding (DWB) via various bonding materials such as epoxy, solder, and glass [8].

DWB, as reported by Gösele *et al.* in 1995, can use ultra-high vacuums (UHV) to limit native oxide formation when bonding GaAs with other semiconductors [9]. Using UHV for DWB barely reduces costs when compared to hetero-epitaxy and does not reduce thermal budgets enough to limit defect generation caused by thermal expansion mismatches between different semiconductors. In another approach, Li *et al.* uses the flux of Indium atoms to bond semiconductor surfaces. However, In increases scattering at the GaAs/Si interface [5].

Unfortunately, current hetero-epitaxy or wafer bonding techniques grow or bond GaAs at $T > 400^\circ\text{C}$ [10]. Due to the large thermal expansion mismatch of GaAs and Si, simply cooling GaAs/Si heterostructures from 400°C to 25°C generates defects at the interface. Thus, $T \leq 400^\circ\text{C}$ and low total thermal budgets for GaAs/Si PV manufacturing are critical to increase the current PV-CE of the tandem solar cell from the present 32.9% to its limit 42.9%, which is 1/2 instead of 1/3 of PV-CE theoretical limits.

2 Issues In Hetero-junction Formation

2.1 Key Issues in State-of-The-Art Hetero-Epitaxy and DWB: High T Oxide Reduction

Bonding GaAs-to-Si has different requirements depending on the application. For example, a wafer-to-wafer bonding method by Zhu *et al.* in 2007 provides void-free, uniform interfaces but uses Sn-Ag solder

[11]. Soldering methods used in microelectronics are inapplicable when manufacturing photovoltaic devices, since metal thin films are opaque and reduce PV-CE.

When DWB methods do not use an intermediate bonding material, $T > 400^\circ\text{C}$ are necessary prior to bonding to eliminate native oxides. Indeed, spontaneous formation of self-terminating native oxides on GaAs and Si surfaces in ambient air is unavoidable and causes defects and carrier recombination at the GaAs/Si interface.

2.2 Recent Advances in Low T Reduction of Native Oxides of GaAs on Si in DWB

Chemical etching, both dry and wet, is the leading low T method used to remove semiconductor oxides as it is conducted at $T = 80^\circ\text{C}$ [12]. Dilute aqueous Hydrofluoric acid HF:H₂O (1–2:20) solutions are well-known to effectively etch native oxides on Si (100) [13]. Most recently, the Herbots-Atluri process has been developed to yield smooth, stable, ordered, and planar passivated Si (100) surfaces where atomic steps and terrace spacing average 20 nm instead 2 nm [14, 15]. These metastable surfaces do not re-oxidize in ambient air, thanks to termination via a metastable, ordered, passivating 2D surface molecular phase of silicon di-hydrate, or Si₂O₂H₄. Si₂O₂H₄ desorbs easily at $T \geq 200^\circ\text{C}$, decreasing oxygen removal by a factor of two [14–19].

In 2006, Bao compared the passivation of GaAs via etching in HCl:H₂O and NH₄OH:H₂O (1–3:10) solutions [20]. Bao showed that aqueous solutions of NH₄OH:H₂O (1–3:10) yield undamaged, stoichiometric, metastable, smooth GaAs surfaces with H⁺-termination. In 2017, Leistner confirmed Bao's results [21, 22].

3 Nano-bonding™ And Surface Energy Engineering: A New Model

3.1. A new Low T ($\leq 220^\circ\text{C}$) Bonding Based on Advances in Wet Chemical Etching

The above advances in wet chemical etching have paved the way for Nano-Bonding™ (NB). The model for this work's approach is low temperature NB, which can lower thermal budgets for DWB to $\leq 220^\circ\text{C}$ and wafer pair compression to $P \leq 60$ kPa (9 psi). NB lowers thermal budget via Room Temperature Surface Energy Engineering (SEE) for compound semiconductors [9, 18, 19, 23–25].

SEE modifies initial total surface energies, γ^{T0} , to far-from-equilibrium states, γ^{T*} , so direct cross-bonds between two different crystals can occur via direct donor-acceptor interactions between SEE-modified surfaces. SEE must be optimized for each material pair for cross-bonding with minimal thermal activation and compression.

SEE typically modifies the γ^{T0} and initial hydro-affinity (H-A⁰) via room temperature dry- or wet- chemical etching, planarization, and termination. Hence, the aim of NB is to optimize SEE. In the present work, SEE optimization is based on the recent reports to nucleate metastable 2D Precursor Phases (2D-PP), that are highly planar at the nano- and micro- scales. 2D-PPs should be as stable as possible in ambient air and only become reactive when contacted with each other due to the engineered difference in polarity

between the surfaces. Such engineered complementary 2D-PPs can then cross-bond by nano-contact via direct electron exchange, ionic species exchange, and van der Waals interactions from the donor 2D-PP surface to the acceptor one. Here, the NB model and optimized SEE are applied in DWB of GaAs to Si for tandem solar cells because this application has the most significant need for low T processing as discussed above. In the present work, the Herbots-Atluri process on Si (100), which yields an ordered, hydrophobic surface, is modified to optimize 2D-PPs on Si (100) in synergy with the passivation etching of GaAs (100). Dilute aqueous $\text{NH}_4\text{OH}:\text{H}_2\text{O}$ (1–3:10) solutions can terminate GaAs with H^+ and are used to investigate whether low temperature NB of smooth Si and GaAs surfaces yields bonding. NB is characterized via Surface Acoustic Microscopy (SAM) and cross-section Transmission Electron Microscopy (TEM), which are used to image bonded GaAs/Si interfaces.

SEE's goal is to develop a chemical method to reduce oxides and passivate surfaces with 2D-PPs at $T < 200^\circ\text{C}$ on both Si and GaAs to prevent damage from plasma oxide removal and processing at $T > 400^\circ\text{C}$, thereby improving the PV-CE of GaAs/Si tandem solar cells.

3.2 Nano-Bonding™ and Surface Energy Engineering (SEE) at $T \leq 220^\circ\text{C}$

Scientific literature shows that state-of-the-art GaAs to Si integration via hetero-epitaxy and DWB requires $T > 400^\circ\text{C}$ [9]. But improving the PV-CE of tandem solar cells requires lowering T to $< 400^\circ\text{C}$.

NB is a new DWB process at $T \leq 220^\circ\text{C}$ [9, 18, 19, 23–25]. NB uses SEE to cross-bond wafers at the nano-scale and 2D-PP to modify $\gamma^{\text{T}0}$ and H-A^0 by bringing each surface in the wafer pair to synergistic 'far-from-equilibrium' states [14, 15, 17, 24, 26].

Far-from-equilibrium surfaces can react with each other and bond via direct nano-contacting with low thermal activation and compression. 'Nano-contact' means bringing surfaces close at the nanoscale and requires wafer planarization at nano-, micro- and macro-scales to minimize compression and maximize contacted areas, as shown in Fig. 1.d.

Complementary 2D-PPs cross-bond upon nano-contact in NB by reacting via donor-acceptor interactions. Optimized SEE can turn the initial HA of *hydrophobic* surfaces into *hydrophilic* surfaces and vice versa. At the same time, optimizing SEE can raise the initial $\gamma^{\text{T}0}$ to 'far-from equilibrium' $\gamma^{\text{T}*}$ and vice-versa. The NB model and SEE are designed by comparing surfaces and NB before and after SEE [24]. Figure 1 shows four such experiments. Fifteen (Fig. 1.a-b) to thirty (Fig. 1.f) metered $10\mu\text{L}$ drops are used along three rows- parallel to the major flat axis- to map γ^{T} across the wafer diameter via Three Liquid Contact Angle Analysis (3LCAA) using the contact angles from three different liquids. Contact angles can be used to compute the three components of $\gamma^{\text{T}0}$ and $\gamma^{\text{T}*}$ using the van Oss-Chaudhury-Good (vOCG) theory [25]. Since SEE renders surfaces metastable and reactive on contact, electrical carriers transfer from donors to acceptors upon contact and catalyze the formation of 2D bonding molecular *interphases*, depicted in Fig. 1.e.

Wetting flattens drops to be large and ~ 10 mm in diameter on the left after SEE on GaAs as shown in Fig. 1.c. The image reveals that the surface is strongly hydrophilic after SEE.

In contrast, the six drops on the right in Fig. 1.c on 'As-Received' GaAs before SEE, show that GaAs native oxides are hydrophobic. H_2O drops bead consistently on GaAs native oxides into symmetric hemispheres averaging a much smaller 4.5 ± 0.3 mm in diameter than on GaAs after SEE, revealing stark differences in HA and γ^T before and after SEE.

As-received 3" Te n + GaAs (100) yields a $\gamma^{T0} = 33.4 \pm 1.1$ mJ/cm² when averaged across 50 mm diameter on both sides of double-polished 3" wafers.

Comparing γ^{T0} maps between both polished sides of 3" GaAs in Fig. 1.b and two 2" n+-GaAs wafers in Fig. 1.c shows that all four γ^{T0} averages are identical at 33.45 ± 0.05 mJ/cm² within a relative error < 0.15%.

The average was calculated using a total of 60 metered drops and 240 measured contact angles. Four angles are extracted per drop using triple points on the left and the right of a drop and its reflection as shown in Fig. 1.g.

Such low relative variation indicates that dopants do not affect GaAs native oxide γ^{T0} unlike on Si [35].

4 Experimental Procedure

NB uses SEE to remove native oxides and planarize wafer surfaces by reducing macro-scale wafer warp and both nano- and micro-scale roughness. At the same time, SEE modifies γ^{T0} and HA^0 to bring surfaces into a 'far-from equilibrium' state and terminate surfaces with 2D-PPs. When 2D-PPs come into nano-contact under mechanical compression between 35 to 60 kPa, molecular cross-bonding is catalyzed via electron and/or ionic species exchange and form a cross-bonding *interphase*.

The initial, "as-received" γ^{T0} and HA^0 values and their modification into far-from-equilibrium γ^{T*} and HA^* values are measured via Three Liquid Contact Angle Analysis (3LCAA). Oxygen coverage is measured via High Resolution Ion Beam Analysis (HR-IBA), which combined < 111 > ion channeling with the 3.039 ± 0.01 MeV $\alpha(^{16}O,^{16}O)\alpha$ nuclear resonance to achieve a threshold detection of about 0.2 oxygen monolayers ($\sim 10^{14}$ at/cm²) by increasing the signal-to-noise ratio for O in Si by a factor of 1600. Surface oxidation states are measured via X-Ray Photoelectron Spectroscopy (XPS). Two identical wafers are processed for each experimental condition to establish reproducibility.

4.1 Surface Energy Engineering of Si (100) and GaAs (100)

A boat of twenty-five 2" Te-doped n + GaAs (100) wafers cut from the same Czochralski-grown GaAs single crystal ingot labeled numbers 1 to 25 according to their slot location is used. As stated above, wafers are grouped into sets of identical processing conditions to establish reproducibility.

The design of the experiment is as follows. For identification, the simple sequential integer numbers from the boat are assigned to each wafer.

“As-received” n + GaAs (100) wafers are labeled 1 and 2 and come from sequential boat slots 1 and 2. They are characterized by 3LCAA, then a few 7 mm x 7 mm squares pieces for conducting HR-IBA and a few 10 mm x 10 mm square pieces for XPS. Wafers 3 and 4 undergo SEE via etching with the most dilute aqueous $\text{NH}_4\text{OH}:\text{H}_2\text{O}$ (1:10) solution for 10 minutes, then rinsed for 10 minutes in 18 M Ω deionized H_2O . The aqueous $\text{NH}_4\text{OH}:\text{H}_2\text{O}$ solution is effective in minimizing surface roughening and preserving the GaAs surface stoichiometry.

Similarly, numbers 5 to 8 are assigned to four 4" Boron-doped p + Si (100) wafers taken from slot #5–8 in a 25 wafers boat. Two “as-received” p + Si (100) are labeled 5 and 6 and characterized via 3LCAA. The two next wafers undergo identical SEE via a modified Herbots-Alturi process where the final ‘passivation’ etch is conducted with aqueous $\text{HF}:\text{H}_2\text{O}$ (1:20) instead of $\text{HF}:\text{CH}_3\text{OH}$ (1:20) [14, 18, 19].

SEE removes native oxides and passivates Si and GaAs surfaces with OH^- and H^+ termination, respectively. To minimize contamination, “as-received” wafers undergoing SEE are kept and processed in a Class 10/ISO 4 laminar flow hood in a Class 100/ISO 5 clean room. In addition, surface energy measurements via 3LCAA on “as-received” wafers that have undergone SEE are also done in a class 10/ISO 4 laminar flow hood in a Class 100/ISO 5 clean room. Following surface energy measurements, samples are characterized using IBA and XPS a few weeks later.

4.2 Three Liquid Contact Angle Analysis, Surface Energy vOCG theory and SEE

The vOCG theory was proposed in 1989 as a three-component theory for γ^T [9, 18, 19, 23–25, 27]. The theory states in Eq. (1) that γ^T is a simple sum of the surface energy component due to molecular interactions, or Lifshitz-van der Waals interaction energy (γ^{LW}) with the square root of the product of the surface energy component of interactions due to electron donor (γ^+) and the surface energy component due to interaction with electron acceptors (γ^-):

$$\gamma^T = \gamma^{LW} + 2 \sqrt{(\gamma^+ \gamma^-)} \quad (1)$$

The vOCG theory was selected for the GaAs/Si pair as the best model to analyze the γ^T of semiconductor surfaces such as Si and GaAs. It can also reliably be used to analyze native oxides like SiO_2 and GaAs oxides because these solids can exhibit molecular interactions, such as acceptor/donor interactions.

3LCAA can characterize γ^T because in the vOCG theory, the three unknown components γ^{LW} , γ^+ , and γ^- used to compute γ^T can be measured via three different contact angles from three different liquids interactions with the surface, provided these three liquids have well-known surface energies and different molecular dipole moments.

The three liquids used in the present work are (i) 18 M deionized water with one hydroxyl (OH⁻) radical per molecule, 1.8546 D, which has a very high dipole moments (ii) glycerin with three OH⁻ radicals per molecule, which has a dipole moment of 0.02 D and (iii) non-polar α -bromo-naphthalene, a geometrically flat molecule with strong donor/acceptor interactions due to Bromine. Figure 2.a shows the molecular structure of all three liquids.

3LCAA is performed in a class 100/ISO 5 laminar flow hood as shown in Fig. 2. All containers and surfaces are made of electronic-grade poly-propylene, boro-silicate glass, or Teflon to avoid organic contaminants.

Contaminant particulate filtration is critical to both SEE and 3LCAA. Figure 2 shows a schematic of the 3LCAA optical bench inside a Class100/ISO 5 laminar flow hood.

To capture high-resolution images of drops and their reflections, a 20 MP reflex digital camera is mounted on an adjustable polypropylene platform inside the Class 100/ISO 5 laminar flow hood. The platform supporting the wafer is a 6" Si wafer made level via four supporting adjustable nylon bolts (Fig. 2.b). Subsequently, three rows metered 10 μ L liquid drops mapping the largest diameter of each wafer measured are photographed under precise illumination from a full solar spectrum light with ultra-high dark/white contrast and high resolution and analyzed via a specifically developed image analysis software called DROPTM [24]. To extract contact angles from the drop contour and the drop reflection on the wafer polished surfaces, DROPTM uses fifth- order polynomial recursive correlated fits of both the 2D-drop boundary with air and of its reflection, as depicted in Fig. 2.a [24]. DROPTM then computes contact angles as the angle made by the first order computed derivative at the air-liquid solid triple point as shown in Fig. 2.b.

A set of three Young-Dupré equations for the three unknowns, γ^{LW} , γ^+ and γ^- , can be derived by combining Eq. (1) with Young's Equation written for a planar surface geometry in (2):

$$\gamma_S^T = \gamma_{SL}^T + \gamma_L^T (\cos \theta) \quad (2)$$

Equation (2) expresses the relationships between the surface total surface energies at the triple point where the solid, gas (air) and liquid phases meet.

The total surface energies for the three surface phases are γ_S^T for the solid surface, γ_{SL}^T for the solid-liquid interface, and γ_L^T for the liquid phase.

Now, Young's Equation (2) for a fully planar surface can then be rewritten for each of the identified components of the total surface energy according to the vOCG theory as shown in Equations (3) and (4).

The component identified as the surface energy of molecular interactions, γ^{LW} , is written as:

$$(\gamma_L^{LW}(\cos^2 \frac{\theta}{2})) = \sqrt{(\gamma_S^{LW} \gamma_L^{LW})} \quad (3)$$

The energy of so-called polar interactions, γ^{POLAR} is decomposed into the surface energies of interaction for electron donors γ^+ and acceptors γ^- as:

$$(\gamma_L^{POLAR}(\cos^2 \frac{\theta}{2})) = \sqrt{(\gamma_S^+ \gamma_L^-)} + \sqrt{(\gamma_S^- \gamma_L^+)} \quad (4)$$

The total surface energy γ^T can then be computed via Equation (5) at a given position via the known γ^L of the three liquids components, γ^{Water} , $\gamma^{Glycerin}$, and γ^{aBr-n} , and by averaging the four extracted contact angles for each of the 3-10 drops.

$$(\gamma_L^T)(\cos^2 \frac{\theta}{2}) = \sqrt{(\gamma_S^{LW} \gamma_L^{LW})} + \sqrt{(\gamma_S^+ \gamma_L^-)} + \sqrt{(\gamma_S^- \gamma_L^+)} \quad (5)$$

For each of the three interacting liquids with the solid surface, the γ^{LW} , γ^+ and γ^- components of a solid surface can be mapped, and its γ^T can be computed via Eq. (1). Young-Dupré equation combines Young's equation and the vOCG model to correlate surface energy components of the solid, from the surface energy components of the interacting liquid, and the contact angle made by the interacting liquid with the solid surface. Hence, the solution of three sets of Young-Dupré equation yields three unknown surface energy components of the solid surface namely, Lifshitz-van der Waals interaction energy γ^{LW} , the energy of interaction of electron donors, γ^+ , and energy of interaction with electron acceptors (γ^-) to compute total surface energy γ^T of the solid by using vOCG.

DROP™ with an average error of $\leq \pm 1^\circ$ enables precise computation of solid surface energy with an average error $\leq \pm 1 \text{ mJ/m}^2$. Measuring water contact angles to $\pm 1^\circ$ makes possible precise characterizations of hydro-affinities as well.

4.3 Ion Beam Analysis

Absolute Oxygen surface coverage is measured by High Resolution IBA, which combines < 111 > channeling with the $3.039 \pm 0.01 \text{ MeV } \alpha(^{16}\text{O}, ^{16}\text{O})\alpha$ Oxygen Nuclear Resonance (NR), in a 10^{-7} to 10^{-8} Torr vacuum. IBA measure absolute ^{16}O coverage via Rutherford Backscattering Spectrometry (RBS) using α -particles elastic collisions with atomic nuclei. The α backscattering energy scales with the mass of the scattering nucleus. ^{16}O has a lighter mass than Si and GaAs, which limits ^{16}O detection in RBS as the large Si and GaAs substrate signals overlap with the small O^{16} signal from native oxides. However, High Resolution in IBA can be achieved, by channeling the particle beam along Si and GaAs < 111 >

crystal axis. $\langle 111 \rangle$ channeling decreases the backscattering yield of Si and GaAs by a factor 40 to a channeling yield which is 2.5 % of the backscattering yield in an un-channeled, Rotating Random (RR) spectrum. Hence channeling can increase the signal to noise ratio for ^{16}O by 1/2 order of magnitude RR spectra are acquired by rotating the crystal about $\sim 5^\circ$ off the $\langle 111 \rangle$ axis to average backscattering yield in all crystal directions.

Moreover, since the crystal (100) surface plane is tilted to an angle of $\sim 54.75^\circ$ to achieve channeling along the $\langle 111 \rangle$ axis, the geometric thickness sampled within the native oxide by the beam, increases by a factor $(1/\cos 54.75^\circ) = 1.73$. Thus, the magnitude of the O^{16} increase the signal to noise ratio by another 75%. Finally, conducting IBA with 3.039 ± 0.010 MeV $\alpha(^{16}\text{O}, ^{16}\text{O})\alpha$ NR further increases the yield of the ^{16}O signal by an additional NR factor of ~ 23 . NR profiling is conducted in incremental 3 keV steps around the 3.039 MeV resonance energy. At resonance, the ^{16}O signal is simulated by iteratively by matching the ^{16}O signal channeling counts in NR to simulated RR ^{16}O counts, via the simulation software SIMNRA [36].

In summary, HR IBA increases the signal-to-noise ratio by a factor $40 \times 23 = 910$, thus about three order of magnitudes over RBS. Using $\langle 111 \rangle$ channeling instead of $\langle 100 \rangle$ improves O detection by a factor 1600, as can be seen in Fig. 4.a. and Fig. 7.a.

4.4 X-Ray Photoelectron Spectroscopy

XPS is used to measure the bonding states of Ga and As and their relative ratio at the surface before and after SEE. XPS spectra are obtained by irradiating the surface with a 1486 ± 0.7 eV monochromatic X-ray beam. Photoelectrons are emitted from the top $\sim 5\text{--}10$ nm of the surface and analyzed as a function of their binding energy. XPS spectra are fitted via Casa XPS 2.3.19, which computes the relative amounts of an atomic species in its various chemical states via tabulated Relative Sensitivity Factors [28]. XPS detects quantitatively changes in oxidation states of As, by measuring the relative ratio As_2O_5 and As_2O_3 . Four data points are collected on two different samples cut from GaAs wafers before and after SEE to establish reproducibility [23].

4.5. Nano-Bonding and its Characterization

NB uses nano-contacting followed by direct mechanical compression via an optically polished compression disk. The pressures experimented with during NB optimization are varied between 5 to 15 psi ($\sim 35\text{--}100$ kPa), with the aim to minimize GaAs wafer breakage while maximizing nano-contacting and reducing and eliminating wafer warp. In addition, steam pressurization at about 1–3 psi ($\sim 7\text{--}20$ kPa) is used. After NB, bonding between GaAs and Si is tested by debonding under 1–20 psi (7- 150 kPa). SAM is used to quantify the interface areas bonded. Bond gaps are characterized via Cross-Section TEM.

5 Results

5.1 GaAs and Si native oxides

Of four 2" Te n + doped GaAs wafers, two wafers are analyzed as-received before SEE and compared to evaluate uniformity of GaAs native oxides, using combined analysis by 3LCAA, HR-IBA, and XPS. Detailed 3LCAA mapping reveals possible anisotropy effects in the hydro-affinity measured via water contact angles, as shown in Fig. 3.e-f, when compared to the uniformity of Si (100) hydro-affinity mapping. A similar effect is seen for glycerin contact angles in Fig. 3.d. Effects due difference in crystal orientations at the triple point has been observed via 3LCAA in highly anisotropic piezoelectric perovskites and will be further discussed in [24, 32].

However, the combination of all three liquid contacts angles to compute γ^{T0} evens out the effect, so that GaAs native oxides exhibit a reproducible, low γ^{T0} of $33.4 \pm 1.1 \text{ mJ/m}^2$, to $\pm 0.15\%$ when compared to γ^{T0} mapped on two other GaAs native oxides on 3" wafers as shown in Fig. 1 [16, 26]. One of the four wafers, wafer #2 in Fig. 4.a. has two optically visible defects. When defective areas are included, GaAs is in average slightly more hydrophilic with $\gamma^{T0} = 42 \pm 1 \text{ mJ/m}^2$. Defects are expected to increase γ^T . On the other hand, both as-received p⁺ Si (100) wafers are initially hydrophilic with a γ^T of $59.7 \pm 1.7 \text{ mJ/m}^2$, consistent with a large number of previously characterized p⁺ Si (100) [35].

The absolute O coverage measured via HR-IBA on as-received GaAs (100) averages $7.2 \pm 0.5 \text{ ML}$ on n + GaAs before SEE, and $13.3 \pm 0.5 \text{ ML}$ on B-doped Si, before SEE. The Ga:As ratio from HR-IBA at the surface is $\sim 54:46$ by HR-IBA, or ~ 1.17 [16, 23]. The GaAs:O ratio of (1:2) shows there are multiple oxide stoichiometries on the surface, given that Ga_2O_3 and As_2O_3 would yield a ratio of 2:3 (M:O) and As_2O_5 would yield a 2:5 (M:O). XPS yields a 6:4 ratio (GaAs: Ga_2O_3). Analysis of Ga and As 3d by XPS matches closely HR-IBA results and yields a Ga:As ratio of 1.16 to within $\pm 1\%$ [30, 31].

A ball-and stick model of initial GaAs surfaces with 7.2 ML of O composed of Ga_2O_3 , As_2O_5 , and As_2O_3 is depicted in Fig. 6. A ball-and-stick model for GaAs after SEE is in progress [32].

5.2 GaAs and Si Surfaces after SEE

Comparing γ^{T0} in Fig. 3.c and 4.a with γ^{T*} in Fig. 7.a. shows that SEE successfully renders GaAs (100) super-hydrophilic, and doubles GaAs initial γ^{T0} to $\gamma^{T*} = 66 \pm 1 \text{ mJ/m}^2$, which is needed for NB. γ^T increases due to electron donor and acceptor interactions, as its component γ^{LW} increases with SEE by only about 30% from 30 to 45 mJ/m^2 , but γ^+ and γ^- increases dramatically each by an order of magnitude. This indicates a high density of dangling bonds, which correlates along with a decrease in oxidation states detected by XPS and discussed below. Si is made hydrophobic with a γ^{T*} of $48 \pm 3 \text{ mJ/m}^2$ after SEE via a *decrease* in electron donor and acceptors as expected in the Herbots-Atluri process [14–19, 23, 29, 33].

Multiple wafers of GaAs and Si after SEE exhibit a reproducible γ^{T*} as the examples in Fig. 1 show. High Resolution IBA of GaAs within 30 min. of SEE of GaAs is shown in Fig. 7.a. Absolute Oxygen coverage decreases on n+-GaAs from $7.2 \pm 0.5 \text{ ML}$ to $3.6 \pm 0.2 \text{ ML}$ [13, 34]. Thus, HR-IBA shows that SEE decreases oxygen coverage on GaAs by 50%. Critically, the Ga:As ratio does not change after etching [23, 29]. The

50% decrease in O detected by HR-IBA affects primarily the oxidation states of Arsenic. While the same proportion, 20%, of Arsenic atoms remain oxidized after SEE, fewer are bound into the higher oxidation states of As_2O_5 and more into the lower oxidation states on As_2O_3 compared before SEE, by 10%. That 10% decreases of As atoms oxidized into As_2O_5 is the likely cause of the radical change in hydro-affinity, as Ga exhibits no change in the degree of oxidation. HR-IBA detects a lesser decrease in absolute Oxygen coverage from 13.3 ± 0.5 ML to 11.8 ± 0.5 ML, as expected for the Herbots-Atluri passivation [14–19].

Next, XPS reveals that after SEE, the surface GaAs to Ga_2O_3 ratio remains 6:4. But, the As_2O_5 to As_2O_3 ratio decreases by a factor of 2. Arsenic is still 20% oxidized. The reduction of As_2O_5 to As_2O_3 signifies that the same amount of Arsenic is bound to Oxygen, but more Arsenic is bound to three Oxygen atoms rather than five, possibly increasing dangling bonds at the surface by 10% and potentially explaining the hydrophilicity of the surface. On the other hand, Ga consistently presents as 22% oxidized. Notably, adventitious C only affects XPS data slightly, by less than 10%, with a correlation factor < 0.6 [23].

5.3 SAM and TEM Interface Imaging Nano-Bonded GaAs (100) to Si (100)

Nano-contacting is enhanced by mechanical compression using a combination of light steam pressurization of 2–3 psi, and a 1.13 cm^2 optically polished compression disk loaded to yield 60 kPa of uniform mechanical compression.

SAM imaging in Fig. 9.b shows that $98 \pm 1\%$ of GaAs to Si within the 1 cm^2 mechanically compressed area is nano-bonded with few defects. Additionally, Nano-bonding™ extends well beyond the compressed 1.13 cm^2 area circled in red in Fig. 9.a into an almost 7 times larger area, 6.8 cm^2 in size despite a lack of significant compression outside the disk. In other words, 48% of the 3" GaAs wafer surface bonded to Si, by compressing less than 7% of the total surface area of the GaAs wafer. This can potentially facilitate the creation of GaAs/Si hetero-structure at low temperature with low surface damage. Nano-bonding without direct compression can occur due to the reactivity of the complementary 2D-PPs, van der Waals bonding, and indicates that mechanical compression is mostly needed to achieve nano-contacting.

SAM also reveals gaps in nano-bonded GaAs to Si, seen as three large white contrast inner regions inside the black GaAs/Si bonded regions. Bonding gaps appear as macroscopic areas that are several mm in diameter outside the 1.13 cm^2 compression region, but inside the larger black area 6.8 cm^2 . This large area shows GaAs and Si reacted outside the mechanically 1.13 cm^2 compressed region. Several smaller white defects appear related to particulate contamination, indicating that Class 100/ISO 4 is not sufficient and that Class 10/ISO 5 particulate control is most likely required.

The TEM cross-section of an interfacial gap in the GaAs/Si pair in Fig. 9.c reveals how reactive the 2D-PP terminated surfaces are. Inside the bonding gaps, significant oxidation occurs on both Si and GaAs despite $T < 220^\circ\text{C}$.

The three larger gaps seen in Fig. 9.b seem to correlate with areas where the super-hydrophilic GaAs may have retained water molecules, interfering with nano-contacting and NB. During processing, it appears the

two surfaces in these unbonded regions become heavily oxidized, consistent with water catalysis. The thickness of Si oxides reaches ~ 120 nm, while the thickness of GaAs oxides reaches ~ 6.5 nm, as seen in Fig. 9.c. Oxides grown inside these gaps indicate that both GaAs and Si are highly reactive in air after SEE, and how modifying γ^T via 2D-PP shifts surfaces to far-from-equilibrium states. modifying γ^T via 2D-PP shifts surfaces to far-from-equilibrium states.

6 Conclusions

In summary, a new direct wafer bonding method, Nano-Bonding™ (NB), has been investigated and successfully applied to the direct bonding of GaAs(100) to Si (100) in air at $T \leq 220^\circ\text{C}$.

NB is based on designing complementary, far-from-equilibrium 2D surface molecular phases specifically for the materials in the bonding pair, by optimizing Surface Energy Engineering (SEE) in synergy for GaAs and Si to nano-bond at low temperatures.

Successful NB by SEE is achieved via a two-pronged approach. GaAs (100) surfaces are rendered highly hydrophilic by H^+ -termination, via chemical etching of the highly hydrophobic native oxides. NB and SEE relies on pairing hydrophilic surface with hydrophobic ones, and so Si (100) is made hydrophilic.

The 2D-PP surface phases increase the initial surface energy γ^{T0} of GaAs before SEE, to render the surface highly reactive with a far-from-equilibrium γ^{T*} when in contact with Si while keeping the GaAs surface passivated at RT in air so it does not re-oxidize.

Surface energy is successfully measured by 3LCAA to $\pm 3\%$, while Oxygen coverage is

measured by IBA to ± 0.2 ML. XPS detects a decrease in oxidation states GaAs surface oxides. 3LCAA show that SEE can double the surface energy of GaAs from the initial 33.4 ± 1 mJ/m² to 66 ± 1 mJ/m², while reducing native oxides on GaAs by at least 50%, and decreasing Arsenic oxidation states from As^{+5} to As^{+3} by $\sim 10\%$.

Thus, surface energy modification, surface oxygen reduction, and chemical state modifications show that synergistic SEE can be successfully optimized via wet chemical etching to achieve NB.

Despite the presence of surface defects, SEE consistently modifies the surfaces of GaAs and Si to highly reactive, far-from-equilibrium states.

Moreover, nano-bonded interfaces can be imaged via SAM and TEM. They show that the 2D-PP on GaAs and Si are highly reactive, and allowing for bonding both with and without mechanical compression at $T < 220^\circ\text{C}$.

Results supports the hypothesis that SEE and low temperature NB can create less defective, and therefore more efficient, GaAs/Si hetero-structures.

Future work will improve surface drying after SEE under dry nitrogen and investigate the degree of hydrogen termination of the surfaces using IBA via hydrogen recoil, in order to eliminate gaps in the bonded interfaces and limit re-oxidation after SEE. Then photo-voltaic performance will be tested and compared to other recent reports on GaAs/Si heterostructure for photovoltaics [32, 38, 40].

Declarations

Ethics Approval and Consent to Participate This research does not involve Human Participants and/or Animals. All authors confirm their participation.

Consent for Publication All authors consent to Publication.

Availability of Data and Materials The data will be disclosed upon request.

Competing Interests The authors declare that there are no competing interests.

Funding Authors declare this research was supported by SiO₂ Innovates LLC., AccuAngle Analytics LLC., and National Sciences and Engineering Research Council of Canada.

Authors' Contributions All authors have given contributions in conceptualization, experimentation, analysis, and/or article preparation.

Acknowledgements The use of the Ion Beam Analysis for Materials (IBeAM) Facility within the Eyring Material Center (EMC), the support of SiO₂ Innovates LLC, and access to the DROP™ algorithm from AccuAngle Analytics LLC are gratefully acknowledged. Lauren M. Puglisi, graduate researcher in the ASU 3LCAA laboratory, is also gratefully acknowledged for her help in editing and proof-reading the present manuscript.

Compliance with Ethical Standards

Conflict of Interest The authors declare there is no conflict of interest.

Research Involving Human Participants and/ or Animals Not Applicable.

Informed Consent Not Applicable.

References

1. National Renewable Energy Lab (2020). <https://www.nrel.gov/pv/cell-efficiency.html>. Accessed 11 April, 2021.
2. De Vos A, Pauwels H (1981) On the Thermodynamic Limit of Photovoltaic Energy Conversion;. Appl. Phys. 25(2): pp. 119 125. doi:10.1007/BF00901283

3. Yoshikawa K, *et al.* (2017) Silicon Heterojunction Solar Cell With Interdigitated Back Contacts For A Photoconversion Efficiency Over 26%. *Nature Energy* 2, 17032
4. Green MA, *et al.* (2018) Solar cell efficiency tables (51) *Prog. Photovolt. Res. Appl.* 26, 3
5. Li L, Davies A, Linfield E (2011) *US Patent* 9,263,264 B2
6. Pakhanov NA, Andreev VM, *et al.* (2018) State-Of-The-Art Architectures & Technologies of High Efficiency Solar Cells Based On III–V Hetero-structures For Space & Terrestrial Applications. *Opto-electronics, Instrumentation & Data Processing*, 54(2), pp. 187-202.
<https://doi.org/10.3103/s8756699018020115>
7. Li J, Aierken A, Liu Y, Zhuang Y, Yang X, Mo J H, Fan RK, Chen QY, Zhang SY, Huang YM and Zhang Q (2021) A Brief Review of High Efficiency III-V Solar Cells for Space Application. *Front. Phys.* 8:631925. <https://doi.org/10.3389/fphy.2020.631925>
8. Essig S, *et al.* (2017) The One-Sun Conversion Efficiency Of III–V/Si Solar Cells To 32.8% For Two Junctions And 35.9% For Three Junctions. *Nature Energy*, 2, 17144,
<https://doi.org/10.1038/Nenergy.2017.144>
9. Gösele U, Stenzel H, Martini T, Steinkirchner J, *et al.* (1995) *Appl. Phys. Lett.* 67, 3614
10. Najafi K, *et al.* (2008) Wafer bonding. Springer doi:10.1007/springerreference_67916
11. Zhu ZH, *et al.* (1991) *IEEE J. of Selected Topics in Quantum Electronics*, 3 (3), pp. 927-936
12. Passlack M, Schubert EF, Hobson WS, Hong M, Moriya N, Chu SNG, Konstadinidis K, Mannaerts JP, Mannaerts, Schnoes ML, Zydzik GJ (1995) *J. Appl. Phys.*, 77(2) 686
<https://doi.org/10.1063/1.359055>
13. Spierings, GACM(1993) *J. Mat. Sci.* 28, pp. 6261–6273
14. Herbots N, Shaw J, Hurst Q, Grams M, Culbertson RJ, Smith DJ, Atluri V, *et al.* K (2001) *Matls. Sci. Eng. B* 87, 303
15. Shaw JM, Herbots N, Hurst Q, Bradley D, Culbertson RJ, Queeney K (2006) *J. of Appl. Phys.* 100, 104109
16. Herbots N, Xing Q, Hart M, Bradley J. D, Sell DA, Culbertson RJ, Wilkens BJ (2012) *Nucl. Instr. and Meth. in Physics Research, Section B*: 272, pp. 330-333
17. Herbots N, Bradley JD, Shaw JM, Culbertson RJ, Atluri V (2010) *US Pat.* 7,851,365
18. Herbots N, Culbertson RJ, Bradley J, Hart MA, Sell DA, Whaley SD (2015) *US Pat.* 9,0,077
19. Herbots N, Whaley SD, Culbertson RJ, Bennett-Kennett R, Murphy A, Bade M, Farmer S, Hudzietz B (2017) *US Patent.* 9,589,801
20. Bao ZL (2006) PhD Thesis, Simon Fraser University, Epitaxial Metal-Gallium Arsenide Contacts Via Electrodeposition Section: B, page: 1685; 186 pages.
21. Karin L, Mingze Y, Christine D, Steffen O, *et al.* (2017) Aligned Cuboid Iron Nanoparticles By Epitaxial Electro-deposition. <https://doi.org/10.1039/c7nr00908a>
22. Karin Leistner *et al.*(2018) *J. Electrochem. Soc.* 165 H3076

23. Ram S, Chow A, Khanna S, Suresh N, Ark F, Narayan S, Gurijala A, Day J, Karcher T, Whaley SD, Kavanagh K, Herbots N (2019) *MRS Advances*, 4(41-42), pp. 2249-2263
24. Baker B, Herbots N, Whaley SD, Sahal M, Kintz J, Yano A, Narayan S, Brimhall AL, Lee WL, Akabane Y, Culbertson RJ (2019) *J. of Vac. Sci. & Technol. A* 37, 041101
25. Oss CJV, Chaudhury ML, Good RJ (1988) *Chemical Reviews*, 88, 927
26. Herbots N, *et al* (2003) U.S. Pat. 6,613,677
27. Carre A (2007) *J. Adhesion Sci. Technol.*, 21 (10), pp. 961-981
28. Jimbo T, Egawa T, Soga T, Hayashi Y (2005) *Photonics Based on Wavelength Integration and Manipulation*, IPAP Books 2, pp. 25–38
29. Cornejo C, Bertram M, Diaz T, Narayan S, Ram S, Kavanagh K, Herbots N, Day JM, Ark FJ, Dhamdhare A, Culbertson RJ, Islam R (2018) *MRS Ad.*, 3(57-58), pp. 3403-3411
30. Schwartz GP, Gualtieri GJ, Kammiott GW, *et al.* (1979) *J. Electrochem. Soc.* 126, 1737
31. Vancauwenberghe O, Herbots N, Manoharan H, *et al.* (1991) *J. Vac. Sci. Technol.* 9(3), 1035
32. Sahal M, Gurijala A, Chow AA, Khanna S, Suresh NC, Peng W, Balasooriya T, Jandhyala SV, Penmatcha PV, ... Kavanagh KL, Culbertson RJ, Herbots N (2021) To be sub. to *J. Vac. Sci. & Technol*
33. Helsen L, Van den Bulck E, Van Bael MK, Vanhoyland G, Mullens J (2004) *Thermo. Acta* 414. pp. 145–153
34. Queeney KT, Herbots N, Shaw JM, Atluri, Chabal YJ (2004) *Appl. Phys. Lett.* 84, 493
35. Narayan S, Day, JM, Thinakaran HL, Herbots N *et al.* (2018) *MRS Ad.*, 3(57-58), pp. 3379-3390. <https://doi.org/10.1557/adv.2018.473>
36. Mayer M (1999) *Americ. Inst. Phys. Conf. Proc.* 475, p. 541. <https://doi.org/10.1063/1.59188>
37. Sahal M (2019) M.Sc. Thesis, Arizona State University, *Dpt of Materials Science & Engineering*, 'Surface Energy Engineering (SEE) for Direct Bonding of Lithium Niobate to Si-based Materials/'
38. Tamboli AC, *et al.* (2015) *Appl. Phys. Lett.* 106, 263904 <https://doi.org/10.1063/1.4923444>
39. Sahal M, Elison A, Prakash S, Swaminathan S, Rane R, Baker B, Balasooriya, T, Peng W, Gurijala A, Suresh N, Puglisi L, Culbertson RJ, Herbots N (2021) Design and Engineering of Gibbs Free Energy for Heterostructure Nano-Bonding™ of Piezo-Electric Crystals to Si-based materials at T < 500 K. *Bulletin of the American Physical Society*, <http://meetings.aps.org/Meeting/MAR21/Session/X41.5>
40. Sahal M, PhD Thesis (2023), In preparation.

Figures

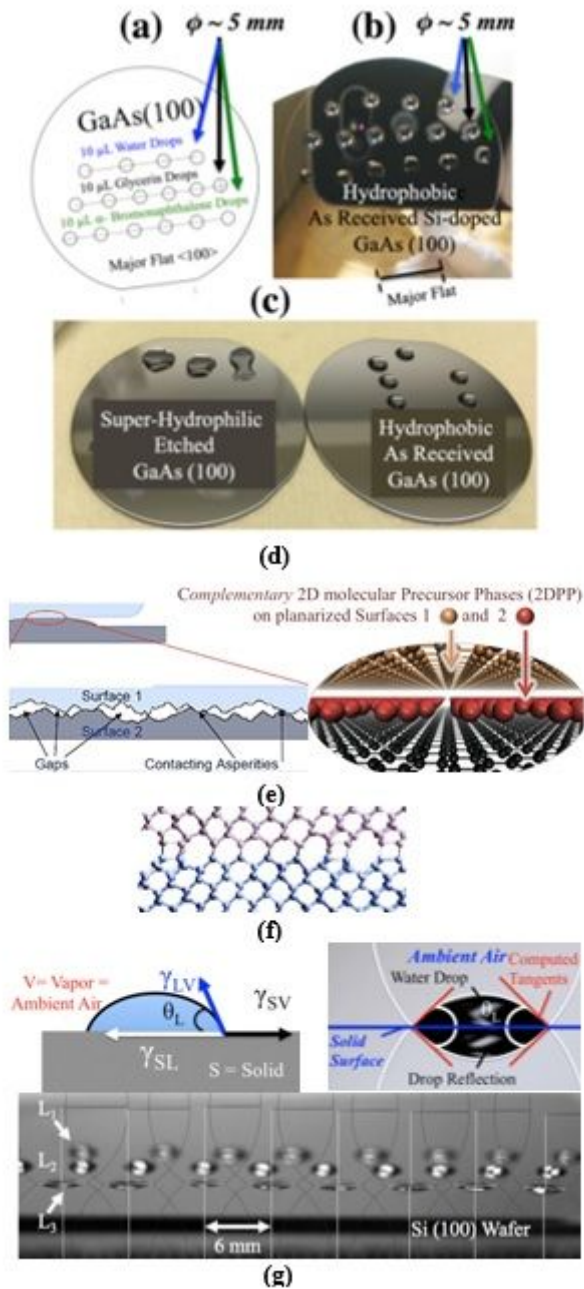


Figure 1

(a) 3LCAA Mapping via 15 metered 10 μL liquid drops to measure γ_{T0} , and γ_{T^*} . (b) 4 drops of 18 M Ω H $_2$ O, 6 of glycerin, and 6 of α -bromo-naphthalene applied on double polish 3" i-GaAs (100), yield $\gamma_{T0} = 33.45 \pm 1 \text{ mJ/cm}^2$ for both sides to $\pm 3\%$. (c) Two 2" n+ GaAs (100) from the same 25-boat. Left: Three 10 μL drops of 18 M Ω H $_2$ O, after SEE. Right: Six 10 μL drops of 18 M Ω H $_2$ O, before SEE. (d) Left: Schematic shows poor bonding due to contacting asperities. Right: Ball-and-stick model for planar 2D-PPs depicts nano-contact. (e) Ball-and-stick model of a continuous interfacial phase, or interphase. (f) Left: Definition of contact angles. Right: curve fitting of contours for a 10 μL drop and its reflection. Bottom: Three liquids are used to map via 3LCAA γ_{T0} across a 4" p+-Si (100) wafer before SEE. (g) Thirty 10 μL drops are used in three rows of 10. Analysis includes drop reflections, and yields 240 contact angles.

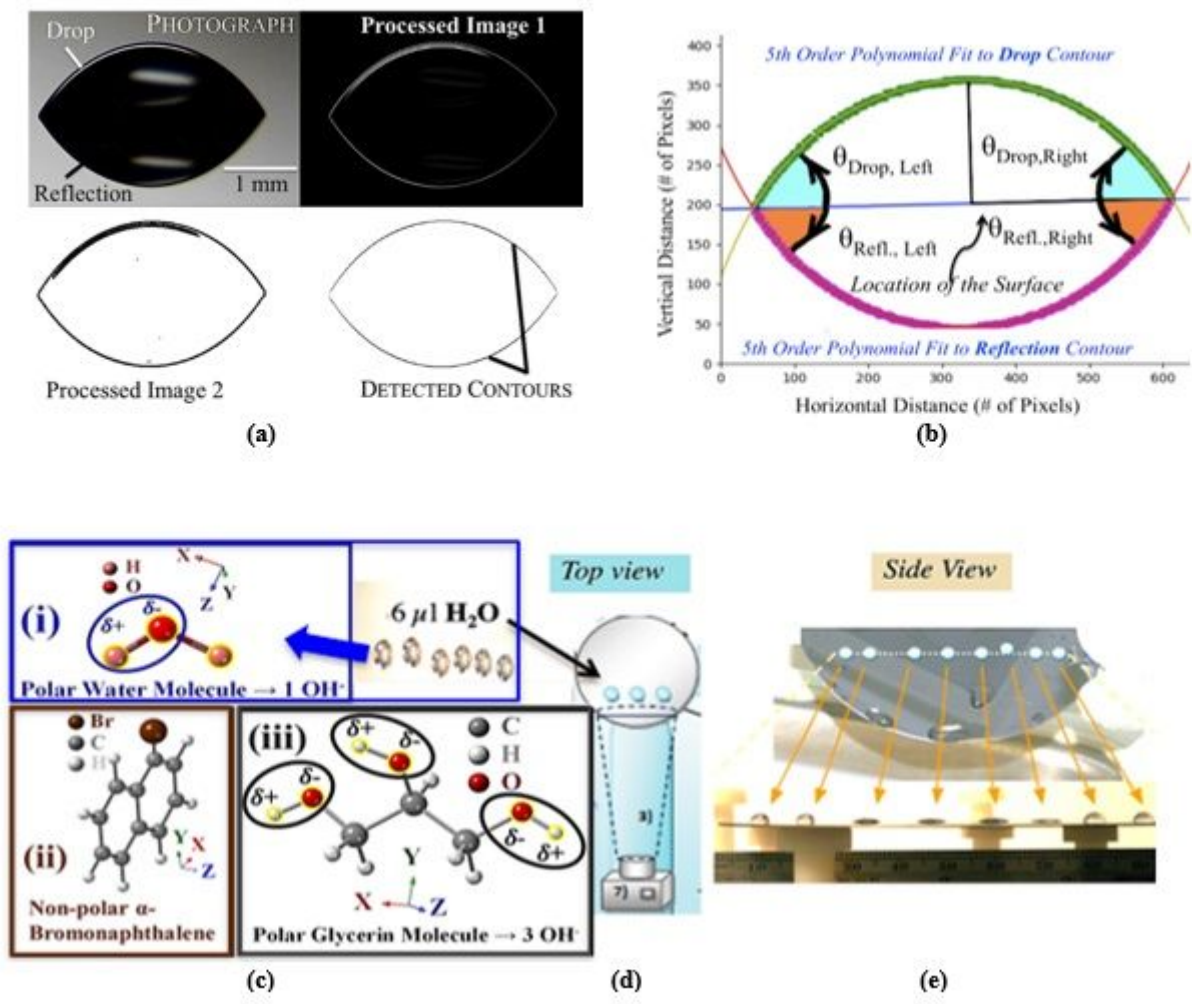
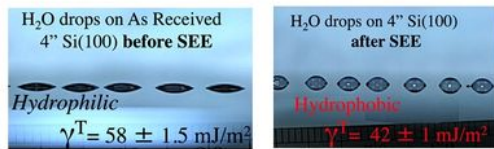
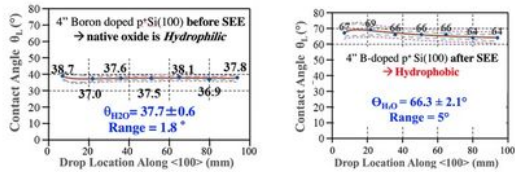


Figure 2

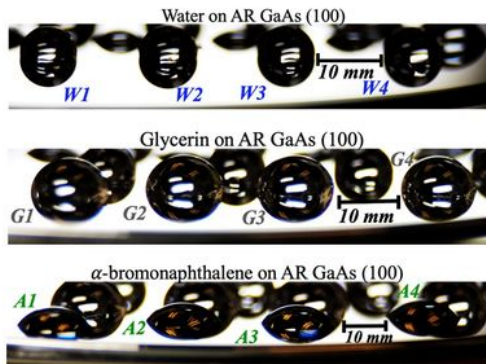
(a) Upper left: Image of a droplet and reflection in 3LCAA. Upper Right and Bottom: Image processing via DROP™ uses 3 steps: Actual contours are used to extract θ_L instead of fitted ellipses. (b) 5th order symmetric polynomials fit contours of the drop and its reflection to extract four θ_L s. (c) Molecular dipoles of the liquids selected for 3LCAA (i) 18 M Ω deionized (DI) H₂O, $p = 1.85$ D, (ii) α -bromo-naphthalene, $p = 0$, (iii) glycerin $p = 1.52$ D. (d) Geometry used in 3LCAA, with imaging field marked in dashed lines, showing how the horizontal median of the camera lens aligned with the wafer edge, with a camera tilt angle of $\sim 0.25^\circ$ above the wafer (100) plane, to capture in a single image of drops and their reflection. The tilt angle causes a variation of $< 0.1^\circ$ between reflection and drops. (e) Top: Mapping via eight 10- μ L H₂O drops of a 4" Si (100) wafer. Wetting is detected in the upper part due Herbots-Atluri processing, NB, and de-bonding. Bottom: Side view of the eight H₂O drops, showing how hydro-affinity is measured via θ_{H_2O} mapping.



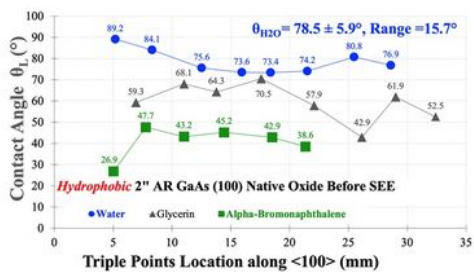
(a)



(b)



(c)



(d)

Surface	Liquid	# of Drops	Average $\theta_{120} \pm \sigma$ (°)	Average $\theta_{90,180} \pm \sigma$ (°)	Average $\theta_{\text{drop, refl.}}$ (°)	Relative Discrepancy Between Drop & Reflection
GaAs (100) after SEE	18 MΩ DI H ₂ O	4	78.5±5.9	80±3.1	79.2±4.5	1.9%
	Glycerin	4	59.7±7.5	57.9±18.7	58.8±13.1	3.1%
	α -Bromonaphthalene	3	40.7±3.5	36.8±12.3	38.8±7.9	10.2%

(e)

Figure 3

(a) 3LCAA Contact Angle θ_{120} on $4''$ p+ Si (100). Left: Five drops wet the 'as-received' (AR) hydrophilic native oxide across 30 mm. Right: After SEE seven drops bead on hydrophobic Si (100). (b) Left: Complete map of θ_{120} across 100 mm on AR $4''$ p+ Si(100) before SEE yields a uniform HA, with θ_{120} averaging $37.7 \pm 0.6^\circ$. Right: After SEE, complete map of

$\theta_{\text{H}_2\text{O}}$ across 100 mm on 4" p+ Si(100) averages $66.3 \pm 2.1^\circ$. (c) Sequential θ_{L} mapping on AR 2" GaAs (100) before SEE yields a γ_{T0} of $33.4 \pm 1.1 \text{ mJ/m}^2$ using (top) four 10 μL drops of H_2O , (middle) five 10 μL drops of Glycerin, and (bottom) five 10 μL drops of α -bromo-naphthalene. (d) For each drop, four θ_{L} are extracted as shown in Fig. 2.b. Averages of left and right θ_{L} s for each drop and its reflection are mapped along the $\langle 100 \rangle$ axis in 28 locations. $\theta_{\text{H}_2\text{O}}$ ranges between 56.4 to 64.1° on 2×2 GaAs (100), maybe due to GaAs anisotropy as a III-V compound. Mono-elemental Si (100) is more symmetric. Even when mapped across 4" p-Si (100) wafer Si (100) yields a variation of only $\pm 0.6^\circ$, while GaAs (100) mapped across 2×2 yields a variation of $\pm 4.5^\circ$ as seen in Table (e). This is further investigated in [32, 39, 40]

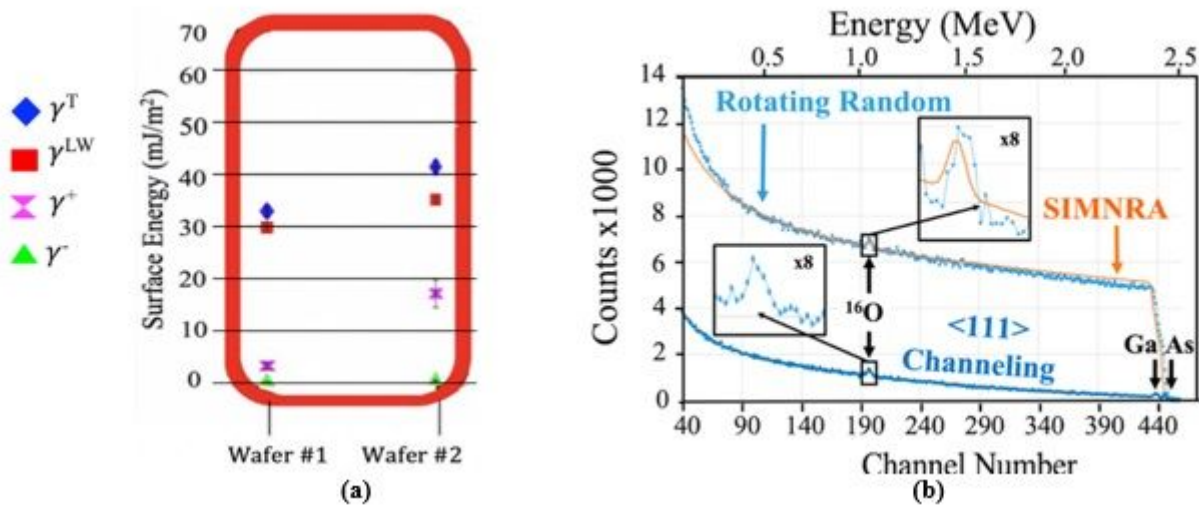


Figure 4

(a) 3LCAA results reveal that as-received GaAs wafer is hydrophobic with $\gamma_{\text{T}} = 33 \pm 1.1 \text{ mJ/m}^2$ and depict the results for the two wafer labeled 1 and 2. γ_{T} is depicted via blue diamonds, γ_{LW} via red squares, γ^+ via pink hourglass, and γ^- via green triangle. (b) High Resolution IBA uses $\langle 111 \rangle$ channeling and Rotating Random spectra taken at $3.039 \pm 0.01 \text{ MeV}$ nuclear resonance $\alpha(^{16}\text{O}, ^{16}\text{O})\alpha$ energy. Channeling spectra are graphed in dark blue, SIMNRA simulations in orange, and RR spectra in light blue [16]

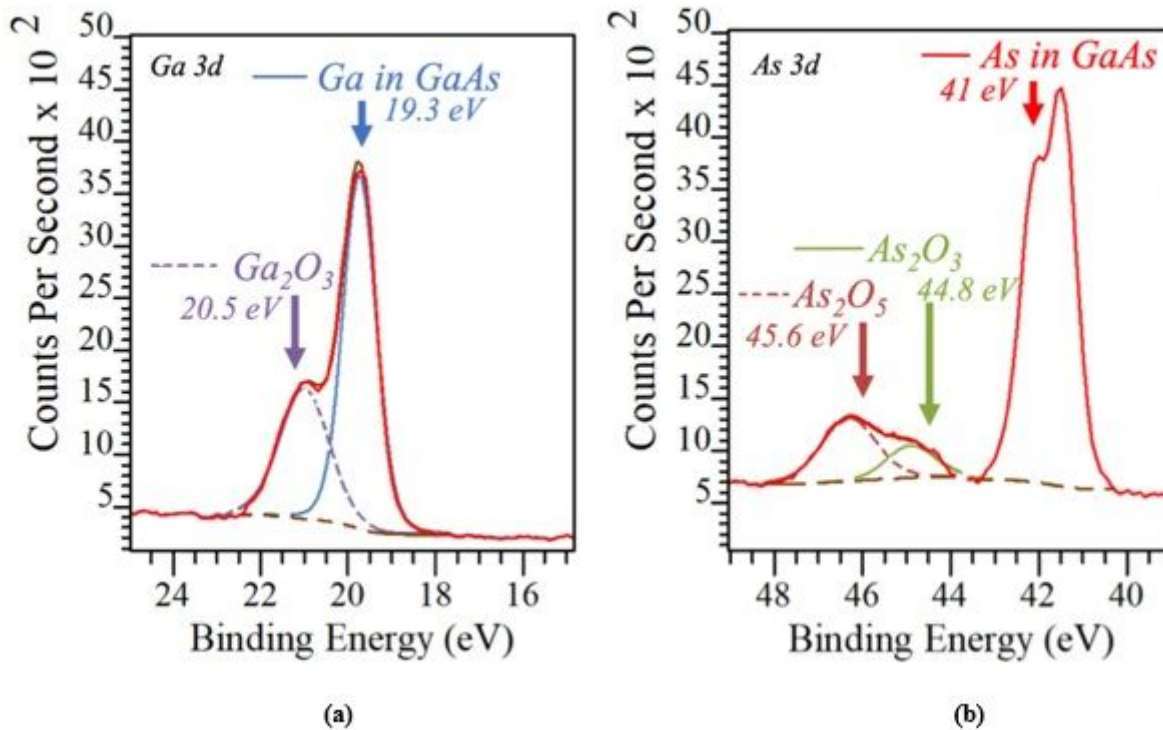


Figure 5

High resolution XPS spectra taken on as-received GaAs (100) include curve fits via CasaXPS 2.3.19 software. The experimental XPS spectra show the distribution of counts in different oxidation states. Raw XPS data is graphed in red. (a) Oxidized Ga is detected as Ga_2O_3 and graphed in purple dashed lines. Unoxidized Ga bound to GaAs is graphed in blue. (b) Oxidized As signals for As_2O_3 are graphed in green. Oxidized As signals for As_2O_5 are graphed in maroon dashed lines. Unoxidized As bound to GaAs is in red [23]

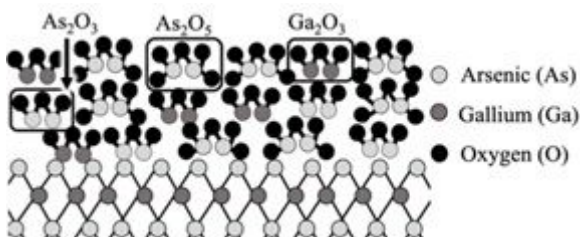


Figure 6

Ball and Stick model of native oxides on GaAs (100) based on five 2" and 3" GaAs (100) wafers characterized by 3LCAA, IBA, and XPS. Their γ_T averages 33.45 ± 1.1 mJ/m². Absolute surface oxygen coverage from IBA averages 7.2 O ML with a Ga:As ratio of ~ 1.17 . Oxidation states from XPS average $\{(5:8:4) [Ga_2O_5]:[As_2O_5]:[As_2O_3]\}$ with 67 bonded O atoms. 20% of As and 40% of Ga are detected as bonded to O via XPS. This can be explained by the fact that GaAs (100) is Arsenic terminated at the GaAs/native oxide interface.

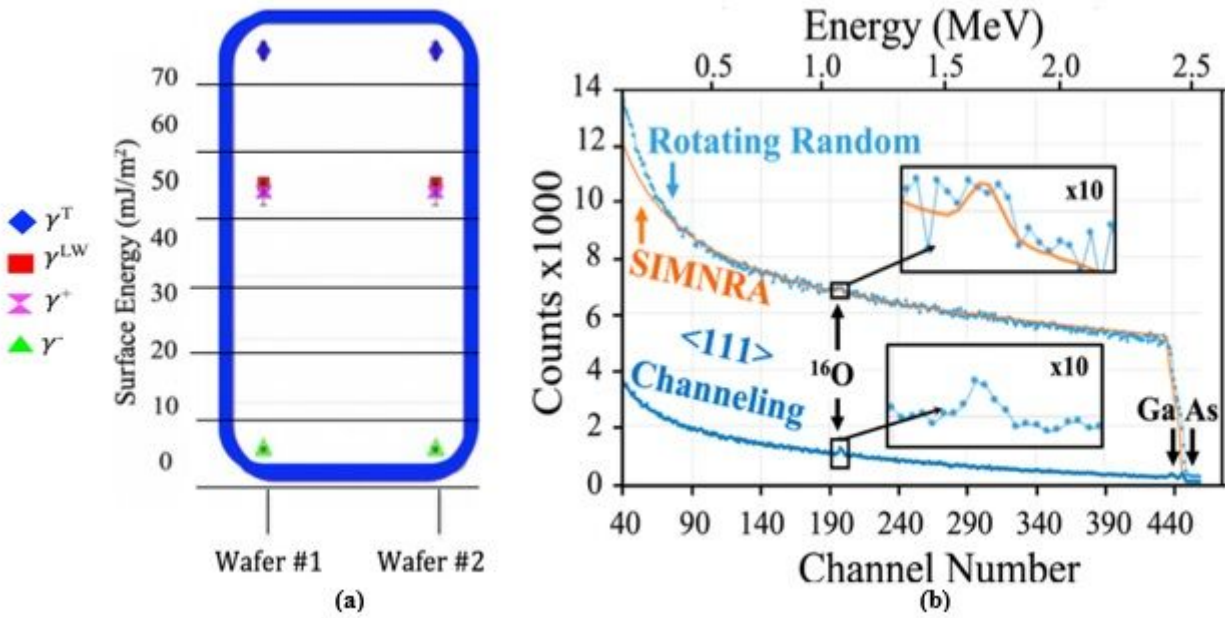


Figure 7

(a) 3LCAA shows that SEE renders GaAs hydrophilic with $\gamma^T = 66 \pm 1.1$ mJ/m² consistently on two identical 2" wafers. γ^T is graphed via blue diamonds, γ^{LW} via red squares, γ^+ via pink hourglasses, and γ^- via green triangles. (b) Both <111> channeling spectrum taken at the 3.039 ± 0.01 MeV NR $\alpha(016, 016)\alpha$ are overlaid, with SIMNRA simulations to extract Oxygen coverage in orange.

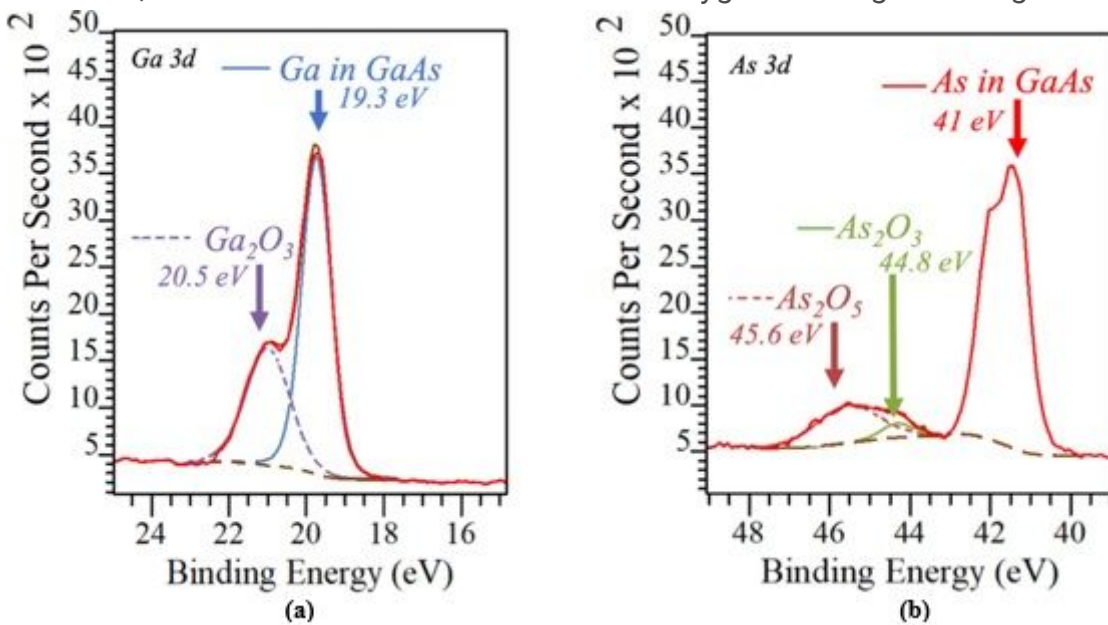


Figure 8

High resolution XPS on GaAs after SEE, fitted via computer simulations using Casa XPS 2.3.19 software and showing the distribution of counts for different oxidation states. Raw XPS data is graphed in red. (a) Oxidized Ga is detected as Ga₂O₃ and graphed in dashed purple lines. Unoxidized Ga bound to GaAs is

graphed in blue. (b) Oxidized Arsenic in As₂O₃ (Tri-oxide) is graphed in green. Oxidized Arsenic in As₂O₅ (Pentoxide) are graphed in maroon dashed lines. Unoxidized Arsenic bound to GaAs is graphed in red [23]

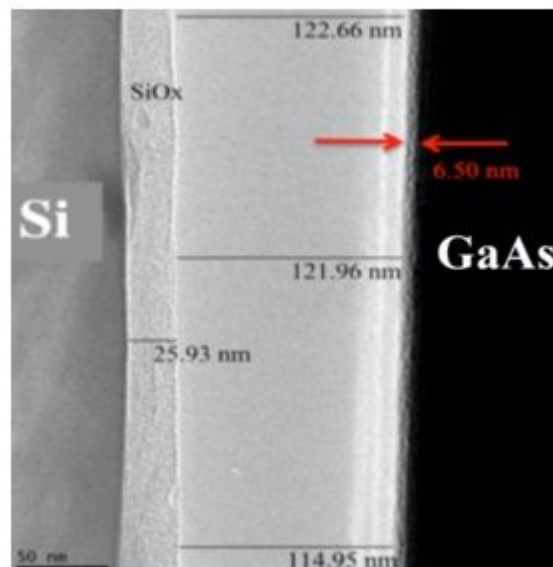
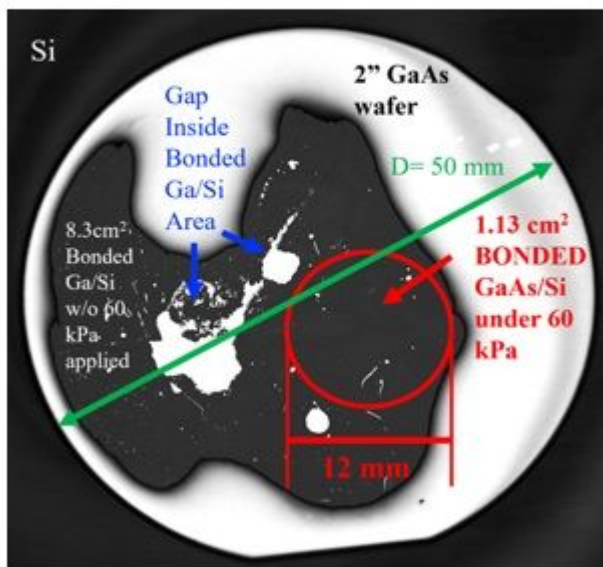
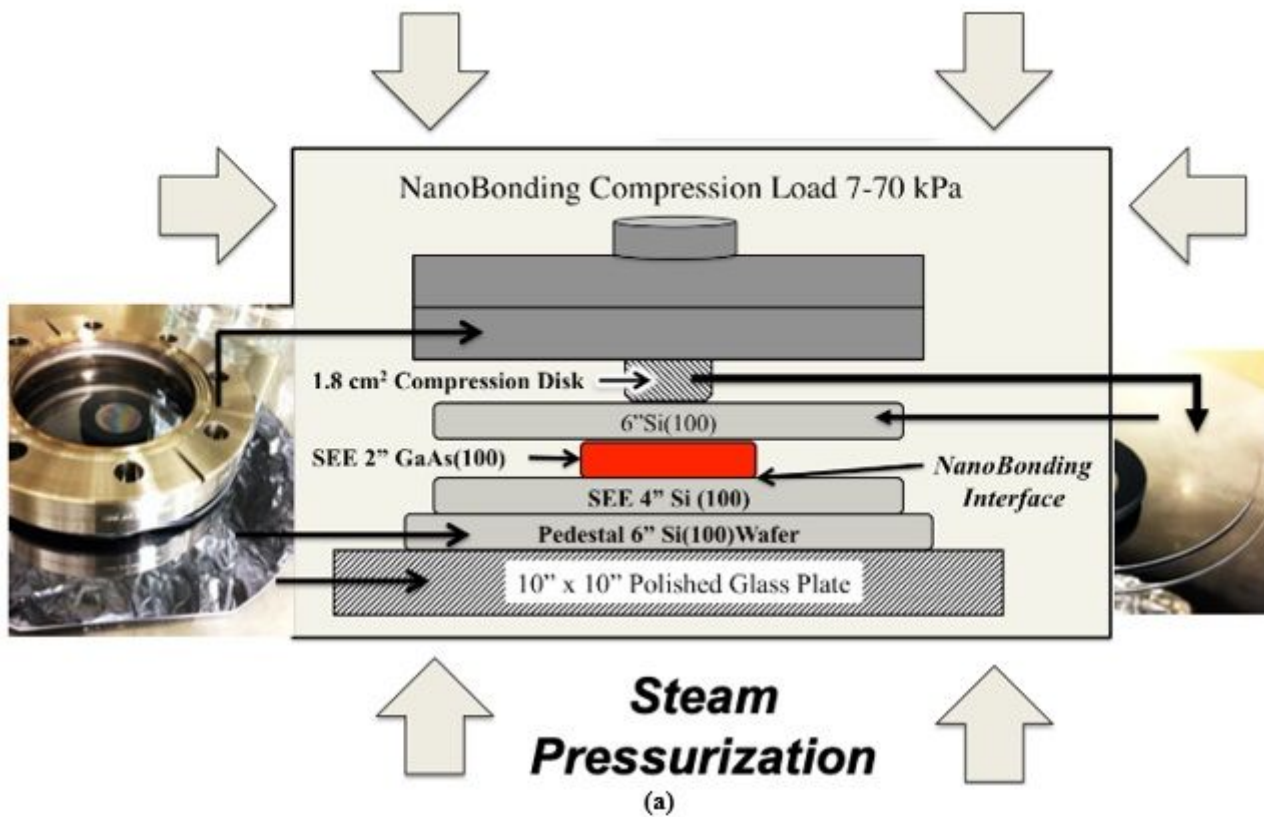


Figure 9

(a) Schematic of Nano-Bonding™ apparatus, used in an oven at 220°C, $p = 7-70$ kPa. A 1.13 cm² optical finish disk [6, 7] is used for compression along steam pressurization represented via grey arrows. (b) SAM imaging of a bonded 2" GaAs and 4" Si wafer. The unbonded 2" circular contour of the GaAs wafer appears as a white disk atop Si. GaAs-to-Si bonded regions inside the white disk are black. Defects

are in white. The 1.13 cm² compression disk is indicated in red, A 98% bonded area of 1.13 cm² is measured inside the 60 kPa compression circle without bonding gaps. (c) Cross-section TEM of an air gap detected by SAM in GaAs nano-bonded to Si.